

Flow Control Applied to the Rounded Front Edges of a Square Prism

Lubinsky Gad and Seifert Avraham

School of Mechanical Engineering, Faculty of Engineering, Tel Aviv University
Tel Aviv 69978, ISRAEL

ABSTRACT

An experimental study of a 2D square prism with two rounded front edges is described. The purpose of the study, performed at roughly 10% full scale Reynolds number is to reduce the aerodynamic drag by means of Active Flow Control (AFC) of boundary layer separation. Highly efficient suction and pulsed blowing (SaOB) actuators array is installed inside a circular cylinder that forms the upper-front curved edge of the model, simulating one of the side-front-edges of a cab. In addition and for simplicity, steady suction is applied at the other rounded corner, both with corner radius to cab width ratio of 0.127. Both oscillatory blowing and steady suction are aimed to inhibit the separation from the front edges. The experimental results show complete suppression of separation, significant decrease in the form-drag, narrowing of the wake and a corresponding increase in the base pressure with the application of AFC. Overall system efficiency is also considered. Future studies will focus on higher Reynolds numbers lower radius corner geometries to improve the usefulness of cab designs.

NOMENCLATURE

AFC	Active Flow Control
AFM 4	Energy Figure of Merit
C_{df}	Front-side drag coefficient
C_{dp}	Pressure drag coefficient
C_l	Lift coefficient
C_p	Pressure coefficient
$-C_{pb}$	Averaged base pressure coefficient (Inverted)
C_s	Nominal suction mass rate coefficient
C_{sm}	Measured suction mass rate coefficient
C_μ	Momentum coefficient
d	Wake width for threshold definition of $0.7 U_\infty$
f	Vortex shedding (dominant) frequency
FC	Flow Control
H	Model height and length
h	Pulsed Blowing Slot (PBS) width
R	cylinder radius
Re	Reynolds number based on $2R$
SaOB	Suction and Oscillatory Blowing
St	Strouhal number based on H
U_∞	Free-stream velocity
u_b	Mean pulsed blowing velocity
x	Horizontal-streamwise location, Free-Stream direction
y	Vertical location
γ	Lower FC device steady Suction angle
γ'	Pressure tap angle – lower AFC device
θ	Upper AFC cylinder Pulsed blowing slot location (angle)

1. INTRODUCTION

Reducing the energy consumption of heavy ground vehicles is an important task. The fuel consumption of these vehicles is extremely high, considering their relatively small number compared to other types of ground vehicles. One of the main reasons for the above is the relatively high aerodynamic drag which characterizes heavy vehicles. Such vehicles are box-shaped which its generic acronym known as a bluff-body. It is characterized by massive separated flow that yields high form-drag resulting from low pressure at the rear surface of the vehicle and in its near wake. Nevertheless, not all the potential for drag reduction is at the blunt-end of the vehicle. The flow could separate from the vehicle's surface just at the edges of its front face, depending mainly on the turning radius, resulting in elevated drag force [1]. The traditional way for preventing boundary layer separation and elevated drag at the front of vehicles is to assure a large enough radius of the front-side edges. This shaping restricts the design space, creates manufacturing difficulties, distorts visibility and more. Current design methodology significantly limits the functionality of the vehicle, restricting the field of view and reducing the internal volume of the cab. Bridging these contradicting requirements could be achieved by Active Flow Control (AFC), a technique capable of preventing flow separation using highly energy efficient fluidic actuators [2]. The use of AFC could relax the stringent design constraints effective nowadays. For example, a numerical study on a truck model shows drag reduction of 10–15% by using oscillatory blowing (synthetic jets) at the aft of the model [3]. For the current application, the no-moving-parts SaOB (Suction and Oscillatory Blowing) actuator, which was proven to be an efficient tool for boundary layer separation control, is used [4–6]. While our group and many other studies focused on the rear of bluff-bodies, simulating the trailer-end, in this paper we discuss the aerodynamic effects of flow control applied to a square prism with rounded front edges using an array of SaOB actuators located at the upper-front-edge and steady suction applied at the lower-front corner. This configuration simulates a cut at mid-height of the vertical-front edges of the truck's cabin. The current paper is a continuation of a previous study that dealt with SaOB actuation applied to the front-edge of a square prism with lower sharp-front corner [7, 8]. The structure of the remaining parts of the paper is as follows: The experimental set-up is discussed next. Following that, results are presented to be followed by discussion and summary.

2. EXPERIMENTAL SET-UP

The experiments were carried out at the low-speed, low-turbulence closed-circuit Knapp-Meadow wind-tunnel at Tel Aviv University. The test section dimensions are 609 mm (width) by 1500 mm (height) by 4250 mm (length). The turbulence level in the tunnel is 0.1 to 0.2%, slightly increasing with the tunnel speed (which is between 3 m/s to 65 m/s). The tunnel free-stream velocity and temperature are measured and controlled by the tunnel computer system.

In order to simplify the complex cab geometry, and still be relevant, the bluff-body model used for simulating the heavy vehicle's front-vertical cabin edges is a square prism with height and length of $H = 300$ mm and span length of $b = 609$ mm, which is also the span of the wind-tunnel test section (Fig. 1a). The rear edges of the model are sharp, while the front edges are round with radius of $R = 38.1$ mm ($R/H = 0.127$, Fig. 1b). The angle of attack of the model was set to zero, meaning that the horizontal surfaces of the model are parallel to the free-stream. The model was located 1200 mm from the test section entrance. The distance between the upper model-surface to the wind-tunnel test section ceiling is 690 mm. The tunnel blockage due to the model installation is relatively large (about 20%). Therefore, it is difficult to quantify the absolute uncertainty of the drag measurements due to sensitivity to Reynolds number of the transition and the separation process. The results therefore should be considered relative to the current baseline, and validated by future free-air or negligible blockage (below 5%) testing and perhaps CFD with and without tunnel blockage effects. Active flow control (AFC) devices were incorporated into the upper and lower front-rounded edges of the model. The lower edge AFC device has the ability to create steady suction and the upper cylinder combines both steady suction and oscillatory blowing. The coordinate system, as well as the actuating locations (which is suction or suction and oscillatory blowing applied at 15 deg apart on the upper cylinder that can also be rotated to move the AFC locations), are shown in Fig. 1b.

The lower AFC device functions as the round-lower-front edge of the model and is capable of creating steady suction through an array of suction holes (Fig. 2). The suction location is altered by taping over the unused holes. The angle between the suction holes' location and the free-stream direction is defined as γ (Fig. 1b). The suction holes span the majority of the part (about 93%). The holes diameter is $d_s = 2.5$ mm,

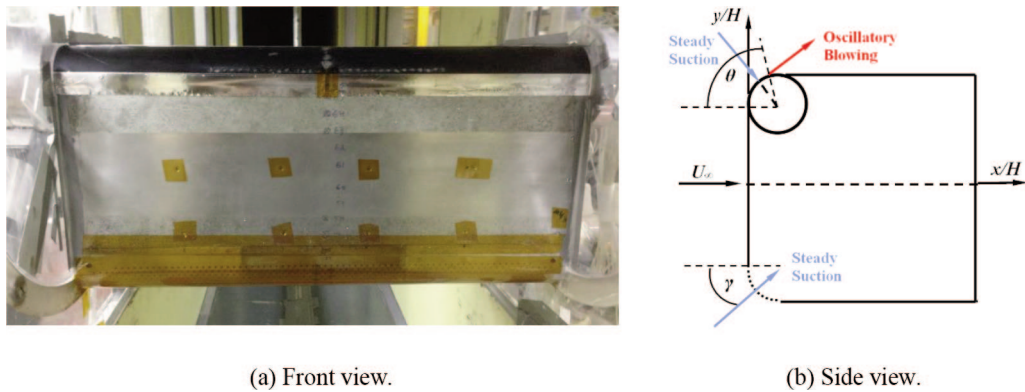


Figure 1. a) The model in the wind tunnel test section (front view). The free-stream direction is into the page. The upper black region is the cylinder, equipped with SaOB AFC actuators and the lower edge (shown covered with Kapton tape) functions as steady suction FC device. b) A side view sketch of the model. The horizontal (x/H) and vertical (y/H) axes are represented by black arrows, the blue arrows are the steady suction (for upper SaOB equipped AFC cylinder and lower suction device). The red arrow is the sideways directed oscillatory blowing of the upper AFC cylinder. The PBS (Pulsed blowing slot) angle, θ , and the location of the steady suction of the lower edge, γ , are also shown. Steady suction on the upper cylinder is applied at $\theta=15^\circ$.

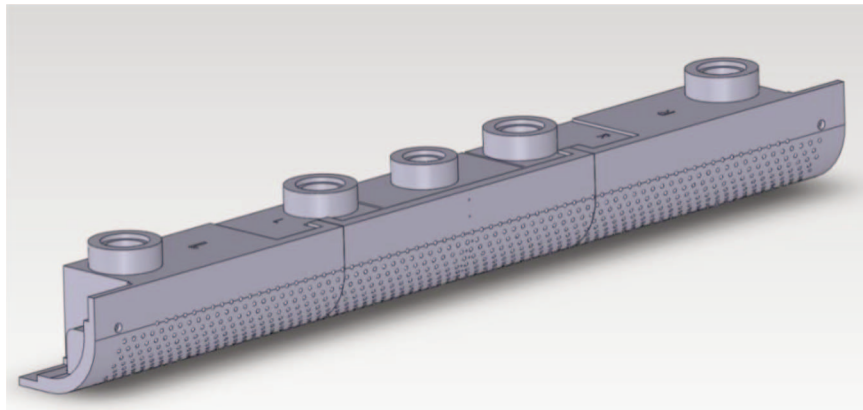


Figure 2. Front view of the assembled parts of the lower round edge steady suction device.

with spacing of 5 mm between holes in the same row (staggered) and 8.18° (γ direction) between the rows, covering $0^\circ < \gamma < 90^\circ$. Therefore, each row contains 76 holes and there are a total of 12 rows. The first and last rows contain only 69 holes, due to design constraints. The suction-pressure is transformed via low pressure tubes that are connected to the suction device. The tubes were connected to a symmetric pressure divider. The mass flow rate, the air density and the sub-atmospheric pressure, were all measured at the entrance (downstream) of the pressure divider. The suction flow was created by an external air pump, which its inlet was connected through the mass flow rate meter to the pressure tubes divider connected to the suction device.

The upper flow control device was in the form of a cylinder composed of two half-circles (Fig. 3a) [4]. A pulsed blowing slot (PBS) of $h = 2$ mm wide was left open, in order to allow the interaction between the actuators' pulsed blowing wall-jets and the external boundary layer flow. An array of 96 suction holes of $d_s = 2$ mm diameter each were drilled almost perpendicular to the surface over the entire span of the cylinder, located 15 degrees upstream of the PBS, as shown in Fig. 3b. The cylinder can rotate around its axis independently of the angle of attack of the model. By that, the PBS location along with the row of suction holes can be altered and its effect quantified. The PBS angle (θ) is defined as the angle between the free-stream velocity (U_∞) direction and the PBS location (as shown in Fig. 1b and in

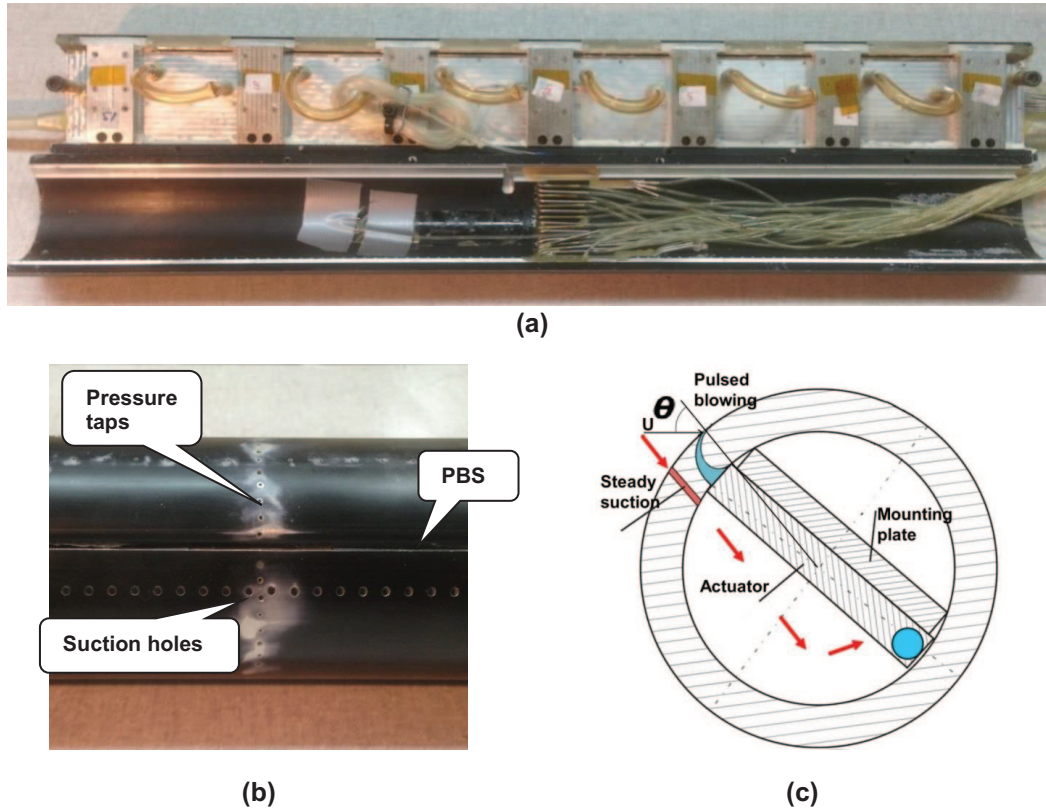


Figure 3. The upper flow control cylinder. a) The two parts of the cylinder taken apart. b) A closer look at the area of the cylinder suction holes and PBS (pulsed blowing slot) exits. Flow direction would be from bottom to top. c) Cross-sectional view of the cylinder. Flow direction is along the U direction. For more details see Ref. 5.

Fig. 3c). The steady suction and pulsed blowing of this AFC device were created by seven Suction and Oscillatory Blowing (SaOB) actuators [4] synchronized at a π phase lag between each neighboring actuator pair (Fig. 3a). The pulsed blowing velocities, suction velocity, SaOB array total power consumption and more, were all based on calibration data made by Hot Wire (HW) measurements [5–9] in a dedicated bench-top set-up.

Pressure taps were positioned at the mid span of the main body of the model, with smaller spacing near the model's corners. Along the perimeter of the upper AFC cylinder, at the half span location, 46 pressure taps were installed with an increment of 7.5 degrees. Only the holes exposed to the flow were considered when plotting the pressure distributions and calculating the integral parameters. Along the perimeter of the round lower edge (Fig. 2), at the middle of its span, 12 pressure taps were installed staggered to the flow direction with an increment of 8.2°. The internal diameter of all pressure taps was 1 mm. The pressure taps locations could be described by the horizontal and vertical axes shown in Fig. 1b. Additionally, the pressure taps around the front curved edges can be described either by the angle with respect to the free-stream direction: θ' is the angle between the free-stream to the pressure tap of the upper FC cylinder and γ' for the lower AFC device. In addition, a few unsteady Endevco™ pressure sensors, with a full scale of 1 psig (6870 Pa), were connected to the model surface, inside the upper and lower AFC devices and two were installed in the wake rake. All the unsteady pressure sensors provide information about unsteady effects, including periodic separation and the vortex shedding phenomenon resulting from it. The wake rake was installed at a distance of 940 mm downstream of the rear surface of the model (where $x/H = 4.13$), for measuring the total pressures at the wake of the model. It includes 60 total pressure tubes and two Pitot static pressure tubes, positioned at the upper and lower edges of the wake rake. The model surface pressures, the wake total pressures and the Pitot tube pressures were acquired by a PSI™ ESP-8400 pressure scanner, with a full scale of either 1 PSI (6970 Pa) or 10" H₂O (2490 Pa) and uncertainty of 0.1% of the full-scale.

Tests were conducted over a range of Reynolds numbers, between 200 k and 500 k, based on the

model height. Baseline measurements were carried out, including taping over the suction holes using adhesive Kapton tape, 19 mm wide and 0.05 mm thick and rotating the upper cylinder FC exits to inside the model to minimize discontinuities. In order to examine the model performance in transitional and turbulent flows, the front side of the model was covered by two strips of a double sided adhesive tape, 0.1 mm thick, 50 mm wide, to which Alumina powder with grain size $k/H = 0.0005$ (Grit #60 roughness) was sparsely spread on (Fig. 1a). The strips were located just upstream of the front rounded edges covering the regions of $0.68 < y/H < 0.85$ and $0.18 < y/H < 0.35$. The roughness strips span the entire model width. AFC tests were performed using a range of actuating magnitudes (altering also the oscillation frequency for the SaOB AFC system) and locations of the upper AFC cylinder (θ) or the lower AFC device (γ).

3. DISCUSSION OF RESULTS

3.1. Asymmetric Steady Suction

The effect of asymmetric steady suction was tested first. For this condition, the upper cylinder FC exits were rotated to be located inside the model and the surface between the upper cylinder and the main model body was smoothed with Aluminum tape. The lower cylinder suction holes were taped over, except for the active suction rows, a pair of adjacent rows each time.

Figure 4 presents the pressure distributions on the lower surface for several suction locations and for the Baseline case (where all of the suction holes are sealed). The Reynolds number is $Re = 0.2 \times 10^6$ and the nominal suction mass flow rate coefficient is $C_s = 0.003$. Where C_s is the normalized suction mass flow rate coefficient, calibrated for no-wind conditions (Eq. 1). In Eq. 1 below, \dot{m}_s is the total suction mass flow rate, U_∞ the free-stream velocity, ρ the free-stream density, H the model height and b is the span length of the model (the tunnel width).

$$C_s = \frac{\dot{m}_s}{U_\infty \rho H b} \quad (1)$$

Note that C_s does not take into account the effect the local static pressure at the region around the suction holes has on the suction flow rates. This effect is later discussed, in conjunction with the data of Fig. 6.

The flow on the upper surface, where flow control (FC) is not applied, is separated just downstream of the front edge for all cases. The pressure coefficient, C_p , is in the range -1.4 and -1.7 , depending on the lower suction angle, γ (not shown). As for the lower surface, where FC is activated, the suction acts to change the flow regime. Observing the Baseline pressure data (Fig. 4), it seems that the

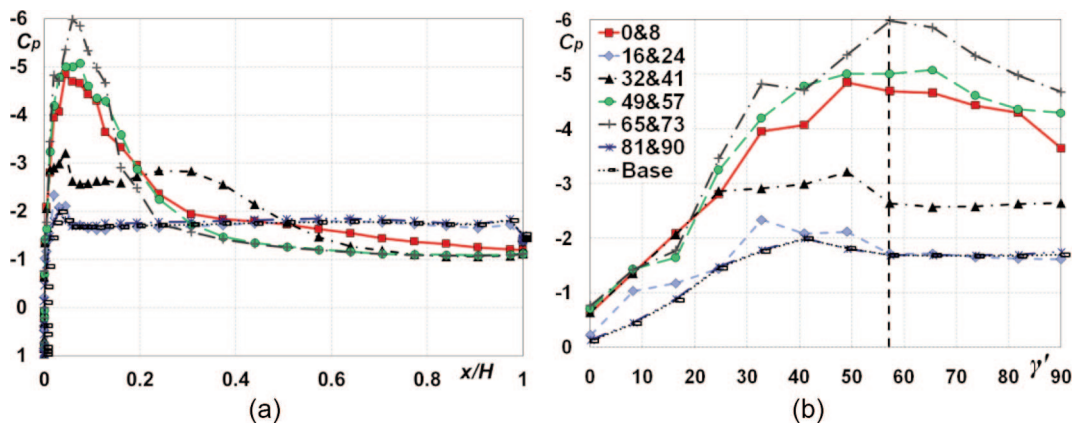


Figure 4. The effect of steady suction (alone) on the pressure distributions over the lower surface, where suction is applied from two rows of holes for several locations over the lower-front curved surface, as indicated in the legend (in degrees). The angle (γ) of the two coupled (to one suction cavity) suction rows which are exposed to the flow is indicated in the legend. Reynolds number $Re = 0.2 \times 10^6$. Nominal suction coefficient $C_s = 0.003$, with the exception of the “Base” where $C_s = 0$. a) C_p vs. x/H (showing the entire model length). b) C_p vs. γ' , only over the curved lower-front edge suction device.

separation takes place at $x/H = 0.058$ or $\gamma' = 57^\circ$. The separation point is identified as the location where the pressure gradient becomes abruptly close to zero, and it remains uniform with x/H . The baseline separation point is marked by the dashed vertical line (Fig. 4b). According to this information, an analysis of the suction angle, γ , effect should be made. For $\gamma = 16^\circ$ & 24° and 81° & 90° , a separation bubble that is open to the wake was formed in a similar manner to the baseline case. However, When activating the suction just upstream of the natural separation point ($\gamma = 49^\circ$ & 57°) or downstream of it ($\gamma = 65^\circ$ & 73°), the suction acts to accelerate the flow. As a result, the separation at the front curved edge is delayed to the rear corner of the model. Consequently, both the base pressure (Eq. 2) and the front side drag coefficient (Eq. 3) decrease (Fig. 5). The total pressure drag coefficient (Cdp), for the current geometry, is the sum of two components $-Cpb$ and Cdf defined as:

$$-C_{pb} = \frac{1}{H} \int_0^H (-C_{p, base}) dy; x_{base}/H = 1 \quad (2)$$

$$C_{df} = \frac{1}{H} \int_0^H (C_{p, front}) dy; 0 < x_{front}/H < 0.127 \quad (3)$$

The wake width parameter d/H , shown in Fig. 5, is the vertical distance in the wake (measured at $x/H = 4.13$) between the two points in which the velocity is 70% of the free-stream velocity, normalized by the model height. For $\gamma = 65^\circ$ & 73° the flow accelerates in a stronger manner so that Cdf is lower, leading also to a lower total drag coefficient. For suction angles further downstream ($\gamma = 81^\circ$ & 90°), the flow for suction magnitude of $Cs = 0.003$ is separated, but for higher suction magnitude of $Cs = 0.0045$, the drag reduces dramatically to a low value of 1.04 (38% reduction, not shown). This behavior makes sense since the suction for $\gamma = 81^\circ$ & 90° is applied too far downstream of the natural separation point and therefore it requires higher suction mass flow rate to reattach the flow.

When applying suction at $\gamma = 32^\circ$ & 41° , which is upstream of the natural separation point, the flow is separated from the model surface, but will reattach further downstream (a separation bubble is formed). Consequently, $-Cpb$ decreases to approximately the same value created by suction applied at $\gamma = 49^\circ$ & 57° and 65° & 73° , but in contrast, Cdf is relatively higher. As a result, the total drag coefficient for this case is slightly higher than for the $\gamma = 49^\circ$ & 57° and 65° & 73° cases. Looking at

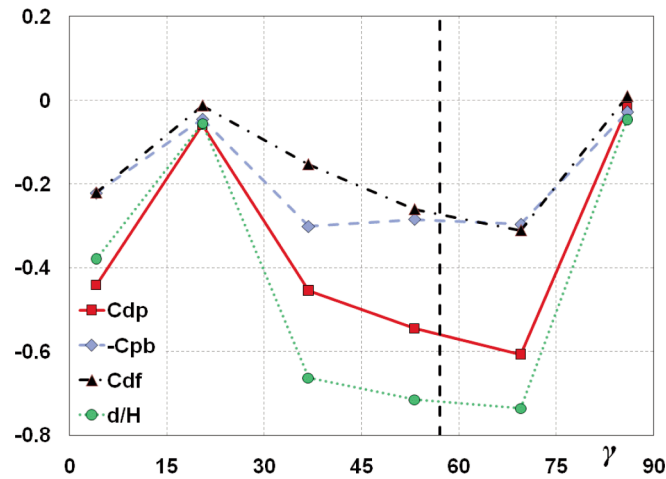


Figure 5. The difference between some integral parameters of the flow (as indicated at the legend) and their baseline values (FC exits are taped over) vs. the average location of the two coupled holes of suction rows which are exposed to the flow, γ . The vertical dashed line represents the separation point ($\gamma' = 57^\circ$) of the Baseline configuration. Reynolds number $Re = 0.2 \times 10^6$. Nominal suction coefficient $Cs = 0.003$. Baseline values are: pressure drag, $Cdp = 1.69$; inverted base pressure, $-Cpb = 1.44$; front side drag coefficient, $Cdf = 0.24$; normalized wake width, $d/H = 1.63$. Negative values indicate reduction relative to the baseline case.

the further upstream suction locations, the trend seems to be different. For $\gamma = 16^\circ$ & 24° , the flow separates just downstream of the curved edge so the total drag is high. In contrast, for suction location of $\gamma = 0^\circ$ & 8° , the flow is attached, leading to low value of C_{dp} , but not as low as the other attached flow cases. In order to better understand these observations, the effect of suction magnitude will now be presented and discussed.

Figure 6a presents the effect of measured suction coefficient, C_{sm} , (with flow ON, taking into account the pressure in the suction cavity with external flow) on the pressure drag for several suction locations. Additionally, Fig. 6b provides the relationship between the measured suction mass flow coefficient, C_{sm} , and the nominal suction coefficient, C_s (calibrated for no-external flow condition). For zero or low nominal suction magnitudes, the measured mass flow rate is negative, meaning that instead of suction, on the average, blowing emanates from the “suction” holes. This behavior can be explained as follows: since the FC exits are located at the front curved-edge where sub-pressure is created on the external surface, pressure that is lower than the suction pressure is created by the pump. Therefore, fluid is actually inhaled into the tunnel through the suction system from the ambient. This phenomenon could have been eliminated by a one-way- valve, but it has not been applied currently. For negative values of C_{sm} , when blowing is actually applied, the drag coefficient is not effected where the FC is activated further downstream of the natural separation point. Observing Fig. 6a, it can be seen that for $C_s = 0$ (or $C_{sm} < 0$), where γ is further downstream of the natural separation point ($\gamma = 49^\circ$ & 57° , 65° & 73° or 81° & 90°), the drag coefficient is identical to the baseline value (be reminded that the natural separation angle is 57°). This insensitivity is probably related to the fact that the suction holes are drilled perpendicular to the curved surface and the blowing magnitude is too weak to create a measurable effect. For $\gamma = 49^\circ$ & 57° , the suction acts to decrease C_{dp} gradually, just for low C_s values, apparently since it is located just upstream the natural separation point. For $\gamma = 65^\circ$ & 73° and 81° & 90° , where suction is applied further downstream of the natural separation point, suction is not effective up to high enough threshold magnitude. This threshold value is sensitive to the suction angle and to the Reynolds number. The abrupt drag reduction for $\gamma = 65^\circ$ & 73° could explain the non-monotonic behavior of the measured suction coefficient (C_{sm}) shown in Fig. 6b. Since the flow abruptly reattaches, the sub-pressure on the external curved edge of the suction device increases, leading to a lower differential pressure between the flow-exposed surface of the suction device to the pump inlet.

The passive effect ($C_s = 0$), of γ located upstream of the natural separation point, has the ability to change the flow regime and it acts to reduce C_{dp} . Furthermore, for $\gamma = 0^\circ$ & 8° and 16° & 24° , the drag is only weakly sensitive to C_s . This finding indicates that the mechanism leading to the above is probably related to transition or enhanced mixing, rather than removing the low momentum boundary layers flow from near the wall. The drag coefficient for these locations, when $C_{sm} < 0$, is lower than the case of $C_{sm} > 0$. The passive effect of the FC openings is to slightly accelerate the flow relative to the suction case. As a result, the inverse base pressure decreases in a weak manner so eventually C_{dp}

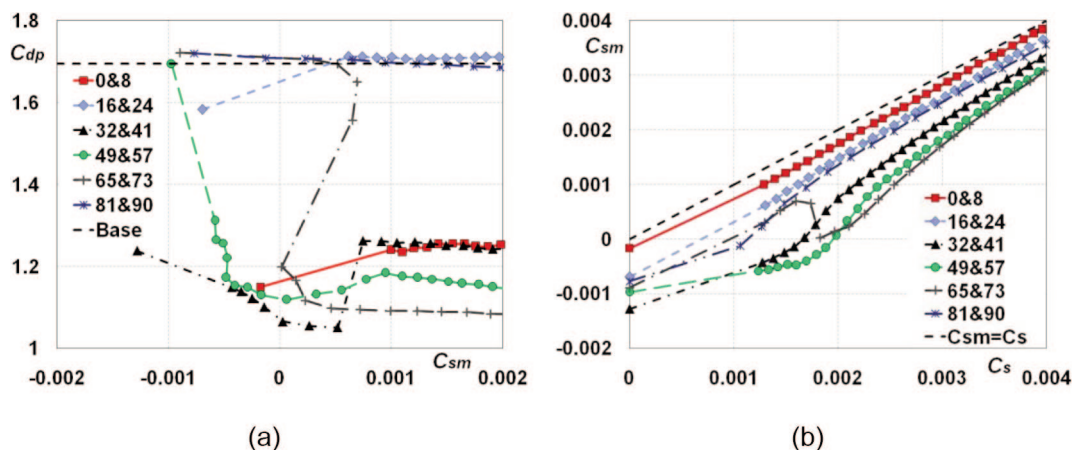


Figure 6. a) The pressure drag coefficient, C_{dp} , vs. measured suction coefficient, C_{sm} . The horizontal dashed line represents the baseline C_{dp} . b) Measured suction coefficient C_{sm} (with flow ON) vs. nominal suction coefficient C_s (calibrated for no-flow conditions). $C_{sm} < 0$ means blowing. Reynolds number $Re = 0.2 \times 10^6$. The open rows of suction holes which are exposed to the outer flow are represented by their angle γ and indicated in the legend.

increase.

A closer look at the effect of AFC created by steady suction is shown for suction location of $\gamma = 65^\circ$ & 73° (Fig. 7, 6b), i.e., downstream of the natural separation position. It can be seen that the flow parameters are insensitive to C_s , up to about 0.002. Increasing the suction beyond $C_s > 0.0015$ (or $C_{sm} = 0.0007$) results in a significant decrease of both $-C_{pb}$ and C_{df} , in addition to the wake narrowing. For $C_s > 0.002$, all of the flow parameters are fixed and are not affected by the increase of the suction magnitude. A comparison between Figure 6a and 7 indicates that though C_{sm} is more physically relevant, C_s provides a more robust and consistent evaluation of steady suction effect on this configuration.

The pressure distributions of the upper surface, which is opposite to the edge where suction is applied, are mostly insensitive to the AFC. It can be seen (Fig. 8a), that for all suction magnitudes, a separation bubble that is open to the wake exists. As for the lower surface (Fig. 8b), the suction acts to accelerate the flow on the curved edge. As a result, for high enough suction magnitudes ($C_s > 0.0016$), the separation is delayed to the rear edge of the model.

Observing the pressure spectra acquired by the unsteady sensors (Fig. 8c & 8d), it can be seen that for low suction magnitudes, where the AFC was not effective, the dominant Strouhal number peak (St is normalized by the model height: $St = f \cdot H/U_\infty$) value is slightly increased with C_s and it is approximately equal to $St = 0.17$. For high enough suction magnitude of $C_s = 0.0018$, the St number increases significantly to 0.25. Further increasing of the suction magnitude will act to increase the St value in a weaker manner to $St = 0.26$ for $C_s = 0.0025$. The sensor located inside the lower-front suction device and the wake sensor pressure spectra are indicating the same dominant St number values. The dominant Baseline peak can only be seen in the wake sensor data, since for this case the suction holes are taped over. Its value is approximately the same as for low suction magnitudes, where suction was not effective; meaning that for too low C_s levels, the suction does not affect the vortex shedding frequency and its strength. Naim et al (2007 [9]) measured similar changes in the Strouhal number based on diameter, while St^* , based on the near wake width was fixed.

The effect of steady suction should be examined for several Reynolds numbers in order to draw general conclusions, not masked by laminar-turbulent transition. For Reynolds numbers of 0.4×10^6 and 0.5×10^6 separation occurs only at the rear-end of the model (not shown) and the front curved upper and lower model surfaces are fully attached. Therefore, in general, the suction will be more effective for low Reynolds numbers where there is a potential for preventing separation from the front edges or when the front edge radii will be smaller such that separation will be present in full scale Reynolds number (around 5×10^6). For Reynolds of $Re = 0.4 \times 10^6$, the effect of suction is different, and can be divided into three main regions. First let us examine the results when suction is located at $\gamma = 0^\circ$ & 8° and

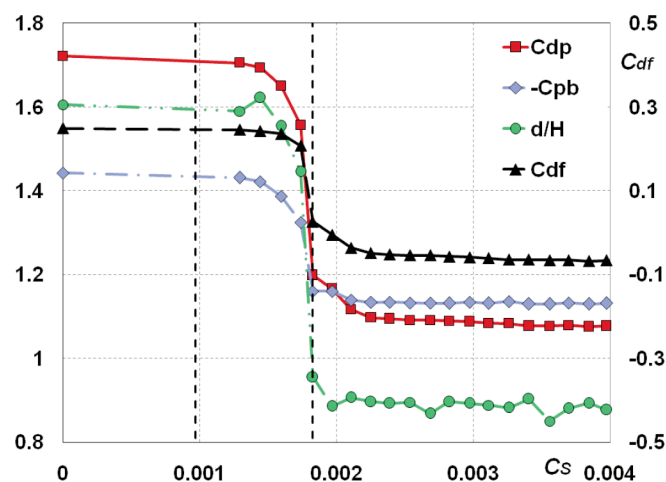


Figure 7. Integral parameters of the flow as mentioned in the legend vs. the nominal suction coefficient, C_s . Vertical secondary (right side) axis refers to C_{df} . The two vertical dashed lines indicate the C_s values where $C_{sm} = 0$ (as shown in Fig. 6b for $\gamma = 65^\circ$ & 73°).

Reynolds number $Re = 0.2 \times 10^6$. Suction is applied at the lower front rounded edge, from $\gamma = 65^\circ$ & 73° .

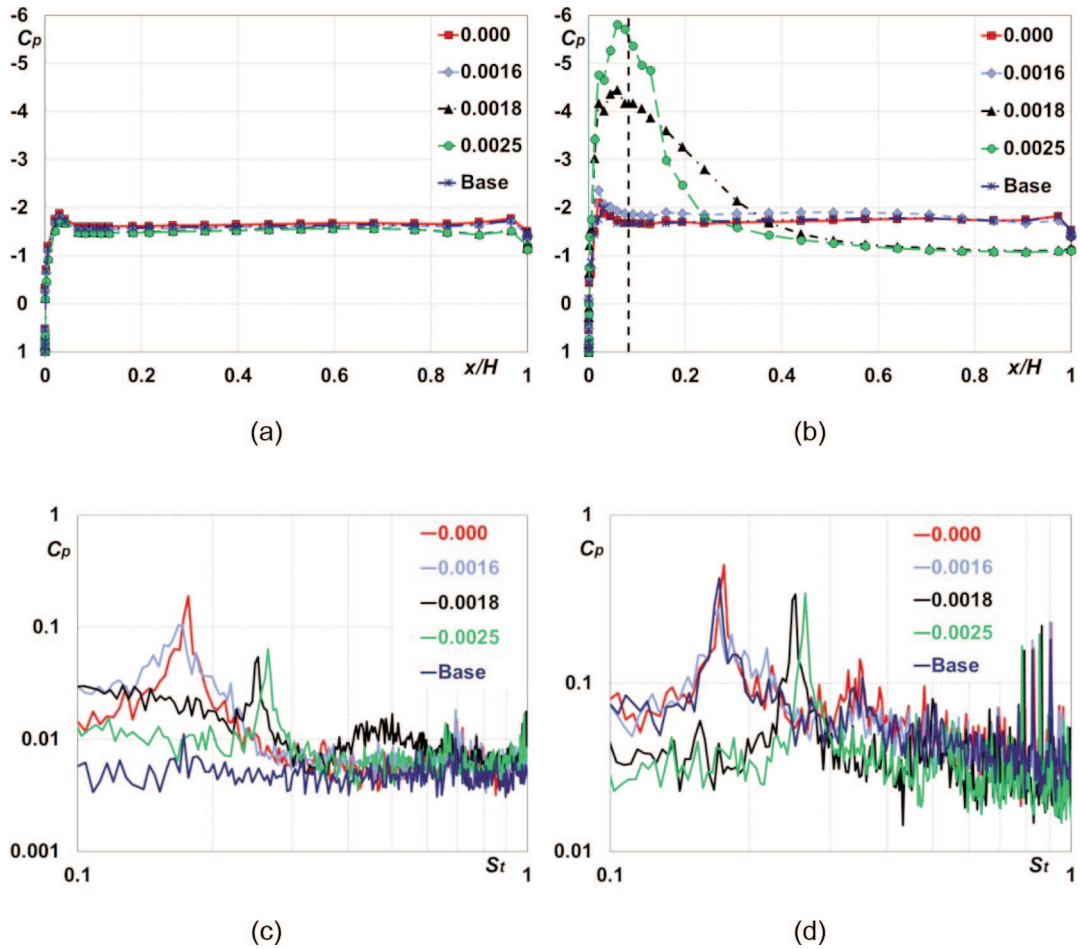


Figure 8. The effect of steady suction magnitude on selected unsteady pressures for several nominal suction coefficients, C_s , mentioned at the legend. Reynolds number is $Re = 0.2 \times 10^6$. $\gamma = 65^\circ$ & 73° . a) C_p vs. x/H on the upper surface. b) C_p vs. x/H on the lower surface where suction is applied. Vertical dashed line represents the average suction location. c) The pressure spectra from an unsteady sensor which is located inside the lower front suction cavity. d) The pressure spectra of an unsteady sensor located in the wake rake (at $x/H = 4.13$; $y/H = -0.58$).

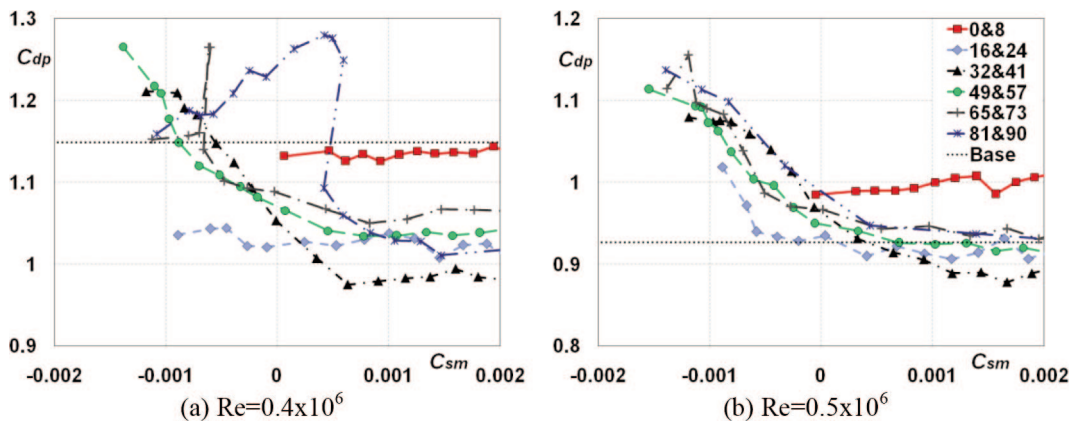


Figure 9. The pressure drag coefficient C_{dp} vs. the measured suction coefficient, C_{sm} . The suction is performed through two neighboring rows which are exposed to the flow and to one internal cavity. The suction angle γ is indicated at the legend. a) $Re = 0.4 \times 10^6$. b) $Re = 0.5 \times 10^6$. Baseline C_{dp} is indicated by a bold dotted line.

16° & 24°. It can be seen (Fig. 9a), that C_{dp} is insensitive to C_{sm} and acts to reduce C_{dp} uniformly when it is applied further downstream ($\gamma = 16^\circ$ & 24°). Second, for $\gamma = 32^\circ$ & 41° and 49° & 57° , the effect of suction is to increase C_{dp} for negative C_{sm} values, relative to the baseline case. With the increase of C_{sm} , the drag coefficient will gradually reduce to a lower value. The effect of suction located at $\gamma = 65^\circ$ & 73° and 81° & 90° is to increase C_{dp} gradually beyond the baseline value for low C_s values. For higher suction magnitudes, the drag coefficient will decrease to lower values than the Baseline case. A maximal drag reduction, close to 15%, can be seen for $\gamma = 32^\circ$ & 41° . For the higher Reynolds number of 0.5×10^6 , the effect of the passive but open suction holes, when on the average blowing is actually applied ($C_s = 0$), is to increase C_{dp} relative to the baseline value. Increasing C_s will act to decrease C_{dp} to approximately its baseline value and up to 5% below the baseline drag for $\gamma = 32^\circ$ & 41° .

3.2. Energy Efficiency

One of the main goals of the current study is to investigate the effect of AFC on the drag force, as active flow control tool, considering the overall energy efficiency. In order to quantify this aspect, and to compare it to different AFC methods and systems, the dimensionless drag coefficients were multiplied by the dynamic pressure, by the reference area and by the free-stream velocity to define the reference power required to overcome the drag. These values assisted us to define drag energy figure of merit, AFM 4 as follows [4, in line with the acronym of this reference]:

$$AFM\ 4 = \frac{W_{d0}}{W_d + W_s} \quad (4)$$

$$W_d = qU_\infty AC_{dp} = 0.5\rho U_\infty^3 bHC_{dp} \quad (5)$$

$$W_s = p_s Q_s \quad (6)$$

Where: W_d (Eq. 5) is the power required to overcome the drag with the presence of AFC and W_{d0} is the power required to overcome the baseline drag (exposing the AFC exits to the flow but without operating the AFC system, $C_s = 0$). The suction power parameter, W_s (Eq. 6) was calibrated for no-flow conditions. Q_s is the total suction flow rate measured at the orifice and P_s is the sub-atmospheric pressure at the entrance to the feeding tube of the pressure divider for the suction device. All measured performance data points with $AFM\ 4 > 1$ indicate increased overall system energy efficiency. The relationship between the actuation power and the free-stream velocity is established through the power coefficient, C_{pwr} :

$$C_{pwr} = \frac{W_s}{qU_\infty bH} = \frac{W_s}{0.5\rho U_\infty^3 bH} \quad (7)$$

Observing the case of $Re = 0.2 \times 10^6$ (Fig. 10a), the AFM 4 is greater than one for three AFC locations. The Baseline drag coefficient is relatively high for most cases, resulting from the flow separation at the front edges. For $Re = 0.4 \times 10^6$, the suction is also effective (up to 20% improvement), but in a weaker manner than the $Re = 0.2 \times 10^6$ case. The reason for the above is that for $Re = 0.4 \times 10^6$, the baseline flow is not necessarily separated (not shown) so the AFC energy effectiveness is accordingly limited. It could be noted that the most effective, minimal C_s to obtain $AFM\ 4 > 1$ is for suction applied at the separation location. The asymptotic behavior of the AFM 4 plot shows a moderate decrease, since the suction power supply is relatively low compared to the aerodynamic resistance. This behavior is important when considering practical applications. Clearly observing Fig. 10b, there is no point in using suction with $C_{pwr} > 0.002$. It should be noted that in practice, the Reynolds number for heavy vehicles are an order of magnitude higher. However, these results can imply that for the case in which the front edge radii are much smaller so the baseline flow is separated and AFC is needed to reattach the flow and reduce drag and the required power to overcome it.

3.3. The effects of Upper-front-corner SaOB Control Cylinder

The effect of the upper cylinder Suction and Oscillatory Blowing (SaOB) active flow control device is described next. Previous study on a square prism with a SaOB cylinder that formed the upper-front

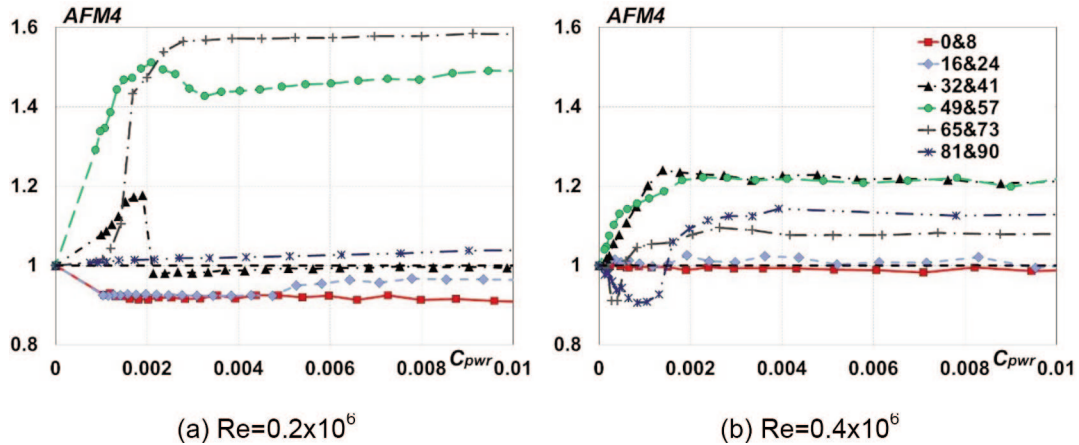


Figure 10. Energetic efficiency (Eq. 4), AFM 4 for different suction angles mentioned at the legend (showing γ). The AFM 4 parameters were calculated from the drag coefficients shown in Fig. 6 and Fig. 9. a) $Re = 0.2 \times 10^6$. b) $Re = 0.4 \times 10^6$.

edge, but with a sharp lower-front edge was performed [9]. The SaOB device was found to be able of preventing separation from the front-curved edge, reducing the drag force and narrowing the wake in an energy efficient manner, for certain conditions [9]. The flow rate of the suction and pulsed blowing SaOB actuator can be controlled by the supply pressure. The actuating magnitude is described here by the blowing momentum coefficient (C_μ).

$$C_\mu = \frac{2h}{H} \left(\frac{u_b}{U_\infty} \right)^2 \left(\frac{7}{15} \right) \quad (8)$$

Observing Eq. 8, h is the width of the pulsed blowing slot, H is the model's height, u_b is the averaged blowing velocity, U_∞ is the free-stream. In addition, C_μ is multiplied by $7/15$ since for this configuration there are only seven out of maximum of 15 SaOB actuators inside the FC cylinder that would cover the entire span of the control cylinder. It should be noted that the suction velocity is about half of the mean pulsed blowing velocity and the frequency increases with the inlet flow rate and pressure, as do the blowing and suction velocities [4].

Figure 11 shows the form-drag variation versus the PBS location for several FC configurations that include: passive effect, pulsed blowing and combining both steady suction and oscillatory blowing, all applied from the upper control cylinder. For all cases, two coupled lower suction holes at $\gamma = 65^\circ$ & 73° are exposed to the flow (passive effect only, the pump is closed so on the average there is no mass transfer). As seen before, this location of $\gamma = 65^\circ$ & 73° at Reynolds number of 0.2×10^6 , has limited passive effect since it is located downstream of the lower separation point. It can be seen that the passive effect of the PBS and the suction holes of the upper control cylinder act to decrease C_{dp} significantly for $\theta = 60^\circ$ and 75° . The effective range of the upper cylinder FC exits ($\theta = 60^\circ$ and 75°) is more downstream than it was for the lower FC instrument ($\gamma = 0^\circ$ & 8° and 32° & 41°). The oscillatory blowing acts to reduce C_{dp} significantly for slot locations of $\theta = 15^\circ$ and 30° . Moving the PBS further downstream, result in a gradual increase of the drag coefficient up to C_{dp} value of the no-FC case, for $\theta = 90^\circ$. Exposing the upper suction holes to the flow acts to reduce C_{dp} in comparison to the Baseline case (34% to 40% drag reduction), regardless of the FC angle θ . Clearly, the added suction is very important for the effectiveness of the current flow control method. It should be noted, in addition, that the characterization of the blowing velocities of the upper FC cylinder was made with open suction exits. Therefore, in practical, the blowing velocity when only pulsed blowing is applied (suction exits are covered) is weaker, since it does not include the added fluid due to the suction. Moreover, the inlet flow-rate and invested power are identical with or without suction.

Observing the pressure distributions presented in Fig. 12, it can be seen that for $\theta = 15^\circ$, where the passive effects of the FC exits are minor, the pulsed blowing acts to accelerate the flow and increase the boundary layer resistance to separation. As a result, separation takes place further downstream

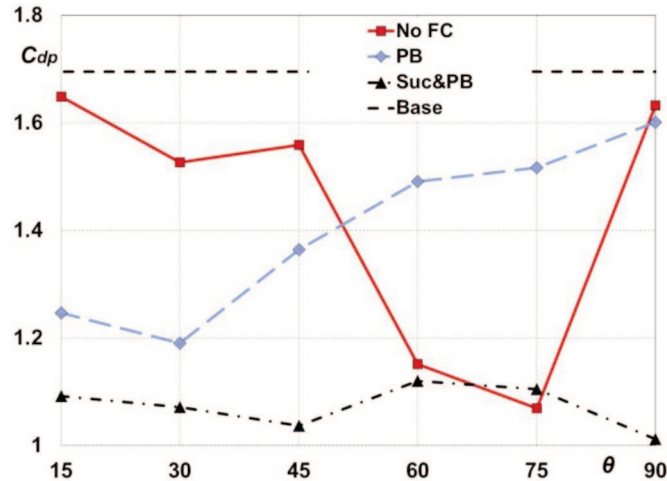


Figure 11. The pressure drag coefficient, C_{dp} , vs. the Pulsed Blowing Slot (PBS) angle, θ , for several FC configurations mentioned at the legend: No FC – upper FC exits are exposed to the flow without pressure supply; PB – suction holes are covered, applying only pulsed blowing through the upper cylinder PBS; Suc & PB – applying both steady suction and oscillatory blowing from the upper FC cylinder. The dashed line represents the Baseline C_{dp} value (taping over the lower suction holes and rotating the upper cylinder FC exits to inside the model). Blowing momentum coefficient $C_{\mu} = 0.014$. Lower suction FC device is not activated. Two coupled suction rows at $\gamma = 65^\circ$ & 73° are exposed to the flow. The suction pump is sealed (leading to $C_{sm} = 0$), $Re = 0.2 \times 10^6$.

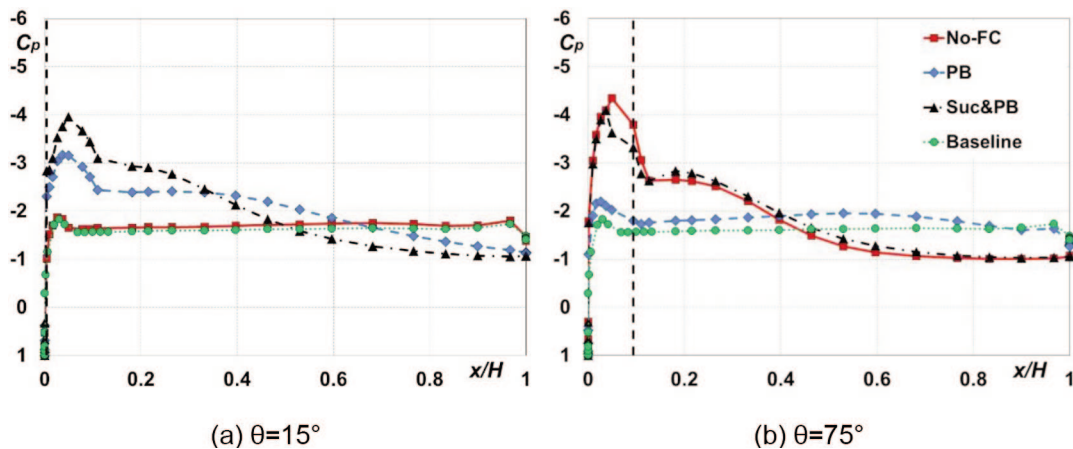


Figure 12. The pressure distributions, C_p , on the upper surface, for several FC configurations, mentioned at the legend (as described in Fig. 11). The vertical dashed line represents the PBS location, $C_{\mu} = 0.014$. Lower-side control device suction is not activated. Two coupled suction rows at $\gamma = 65^\circ$ & 73° are exposed to the flow, but the suction pump is sealed ($C_{sm} = 0$). Reynolds number is $Re = 0.2 \times 10^6$. a) $\theta = 15^\circ$. b) $\theta = 75^\circ$.

(around $x/H = 0.127$), and a separation bubble is created on the upper surface. When opening the upper suction holes, so suction can be applied, the flow accelerates in a stronger manner. Separation takes place at the same point, but the bubble length shrinks and as a result C_{dp} decrease.

For $\theta = 75^\circ$, the passive effects of the FC exits are significant and act to create a separation bubble. Note that at this condition, the suction holes are located slightly downstream of the natural separation point. Nevertheless, when activating oscillatory blowing, the flow separates just downstream the PBS. Combining both suction and oscillatory blowing acts to accelerate the flow, similar to the non-FC case. However, separation takes place at the same location of $x/H = 0.127$ or $\theta' = 90^\circ$. At first sight, this behavior is difficult to explain. However, for this specific model, the surface between the upper

cylinder and the model is not perfectly smooth. This disturbance acts to separate the flow when the boundary layer is not energetic enough or when the boundary layer is quite thin compared to the step height which is between 1 and 2 mm. Therefore, there are two common frontal separation points: One is on the curved edge of the cylinder and the other downstream of it, where the connection between the cylinder and the upper model surface metal sheet is connected. Please note that for the baseline and the steady suction applied to the lower edge configurations, the surface between the upper cylinder and the model was taped over in order to suppress this disturbance.

Figure 13 shows the effect of the upper cylinder FC magnitude on the flow regime when steady suction is applied to the opposite lower front edge. The drag coefficient (C_{dp}) is almost insensitive to the momentum coefficient (Fig. 13a) of the upper cylinder SaOB system. However, its front and rear components are significantly affected by the upper flow control cylinder actuation magnitude. The front-side drag coefficient (C_{df}) decreases with C_{μ} , while $-C_{pb}$ increases. The reduction of C_{df} can be explained by the acceleration of the flow with C_{μ} increasing on the upper curved edge (Fig. 13c). For $C_{\mu} = 0.000$, a separation bubble is formed. For higher magnitude of $C_{\mu} = 0.025$, the separation point is delayed further downstream and the bubble length shrinks as well. For even higher momentum coefficient of $C_{\mu} = 0.051$, the separation is delayed to the rear edge of the model. The actuating magnitude of the upper cylinder does not directly affect the pressure distribution on the lower front edge and lower surface, where steady suction is applied (Fig. 13d). The flow on the lower surface is highly accelerated and it seems that the separation takes place at the rear edge as well. It is interesting to note that $-C_{pb}$ is higher when the flow on the upper surface is fully attached. The fact that the lift

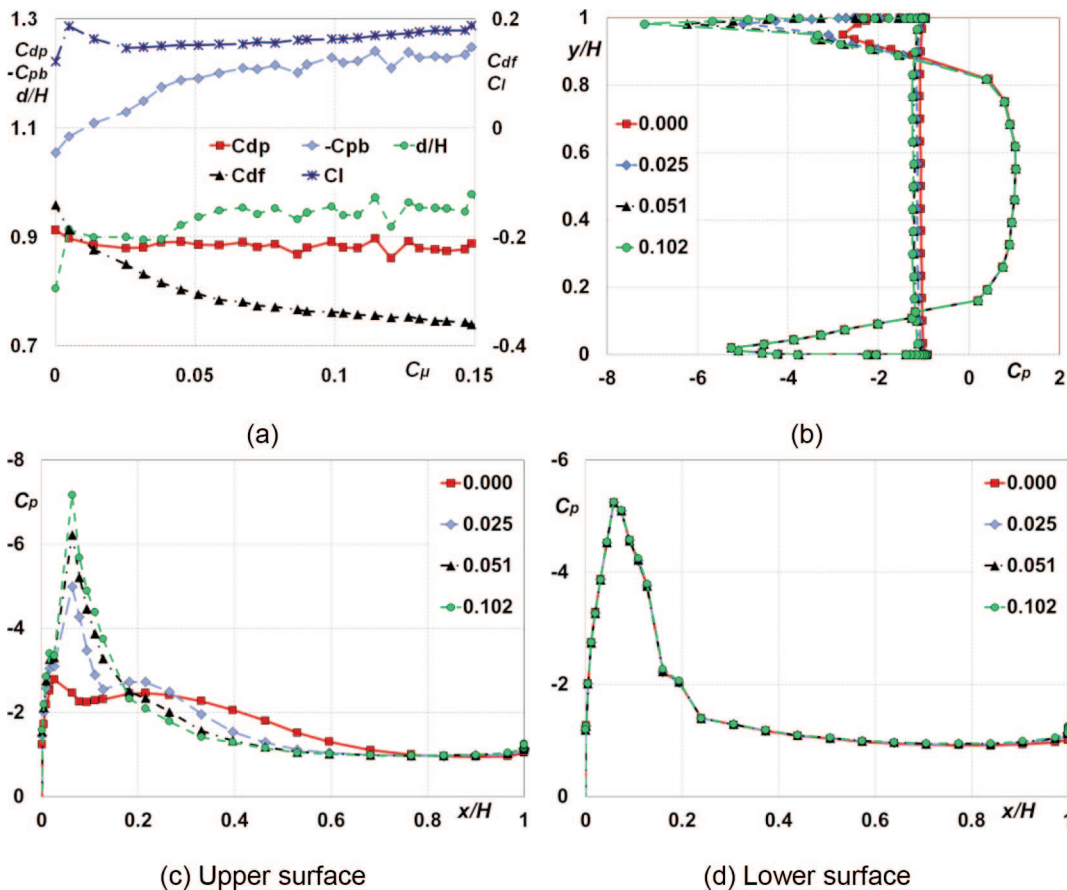


Figure 13. a) Integral parameters of the flow (as indicated in the legend) vs. the upper AFC cylinder momentum coefficient (C_{μ}). Vertical secondary axis refers to C_{df} and C_l . Baseline values (AFC is not applied) are $C_{dp} = 1.69$, $-C_{pb} = 1.44$, $C_{df} = 0.24$, $d/H = 1.63$. b) C_p vs. y/H . c) C_p vs. x/H – upper surface. d) C_p vs. x/H – lower surface. Legend in sub-figs b–d refers to C_{μ} values. The Reynolds number is $Re = 0.2 \times 10^6$. Steady suction is applied to the lower edge device at $\gamma = 65$ & 73° for all cases with suction coefficient of $C_s = 0.0045$ ($0.0037 < C_{sm} < 0.0038$). Upper PBS location is $\theta = 60^\circ$.

coefficient is not zero indicates a non-symmetric flow (Fig. 13a).

The effect of symmetric and asymmetric FC would now be presented and discussed in more detail. For this purpose, the the upper FC cylinder was provided with a fixed pressure supply. Observing Fig. 14a, the AFC applied individually to upper or lower front edges acts to reduce C_{dp} , but the combination of both does not necessarily yields the minimal drag force or the optimal drag reduction. Observing the two components of C_{dp} , which are the inverted base pressure and the front drag force coefficients, it can be seen that for most PBS locations, the combination of upper and lower FC have the undesirable effect to increase $-C_{pb}$ in relation to the one side FC alone. On the other hand, combining FC both on the upper and lower front edges acts to reduce the front drag component, C_{df} . Therefore, the total effect of this combination is relatively close to one side FC. The lift coefficient is shown in Fig. 14b. It can be noticed that for the Non-FC configuration, the passive effects of the upper AFC cylinder is to accelerate the flow on the upper surface such that C_l for most PBS locations is positive. When applying AFC on the upper cylinder the lift coefficient is increased. On the other side, suction at the lower edge acts to reduce C_l . Combining AFC both on at the upper and lower edges yields positive lift coefficient, meaning that a greater sub-pressure is created on the upper surface. In order to better understand these effects, the relevant pressure distributions should be examined.

When AFC is not applied, the flow is separated just downstream of both the upper and lower front-curved-edges at $Re = 0.2 \times 10^6$. Suction on the lower edge acts to prevent separation, but does not directly affects the pressure distribution on the opposite-upper surface. In the same way, activating steady suction and pulsed-blowing on the upper AFC cylinder, acts to accelerate the flow in a way that a separation bubble is formed, but there is no direct effect on the lower edge and the flow remains

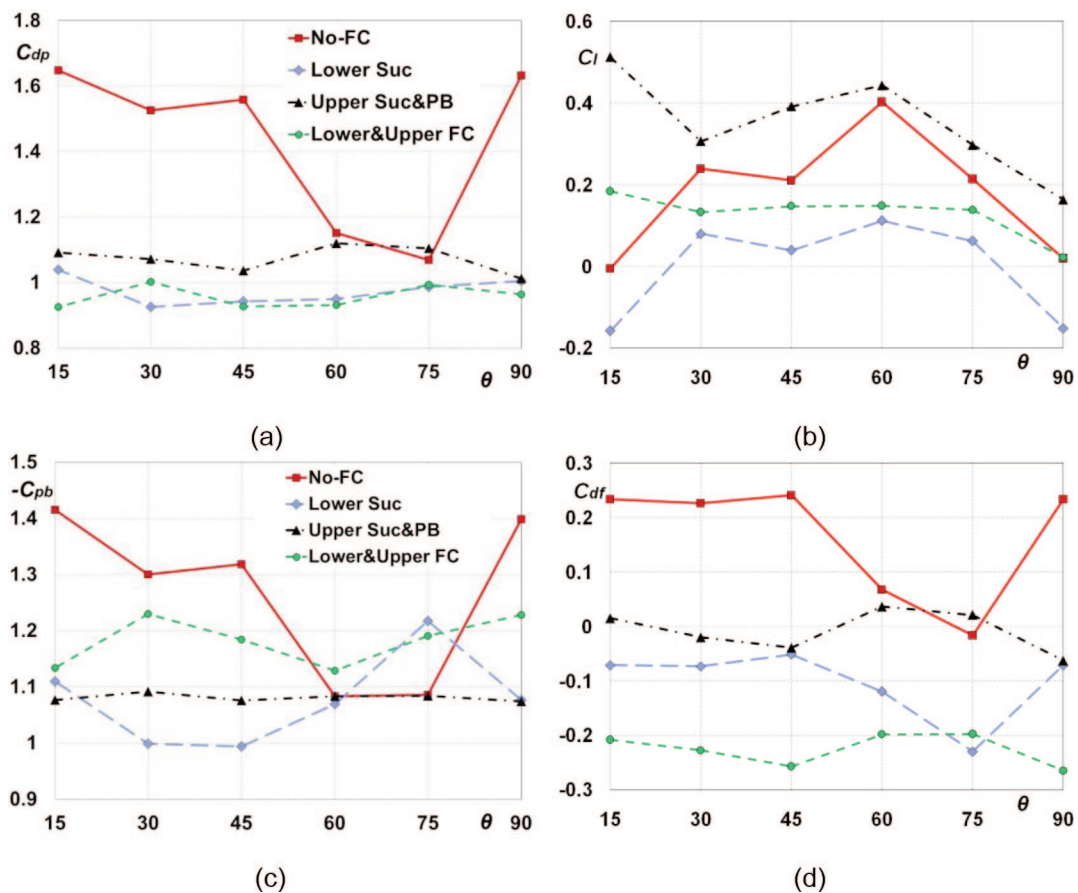


Figure 14. Integral parameters vs. PBS angle, θ , for several FC configurations mentioned in the legend: No FC; FC exits are exposed to the flow without pressure supply; Lower front-edge suction with $C_s = 0.0024$ for all cases. Upper Suc & PB with $C_\mu = 0.014$ and combining both upper and lower FC devices action. Two coupled lower suction rows of $\gamma = 65^\circ$ & 73° are exposed to the flow. The suction pump is sealed ($C_{sm} = 0$ or $C_\mu = 0$) without.

separated just downstream of it. When activating the flow control (FC) devices on both the upper and lower front-curved edges, the FC acts to accelerate the flow for each surface in the same manner as it did for one side activation only. This behavior could easily be explained by the reduction of Cdf when both upper and lower AFC devices are operated. This occurs since on the average, a greater sub-pressure is created on the front edge. However, the base pressure is not necessarily consistent with Cdf . The inverted base pressure for this case is lower when separation occurs from one of the surfaces only. For upper surface FC at $\theta = 30^\circ$, $-Cpb$ is the lowest when suction is applied on the lower surface (Fig. 14c). For this case, the flow is fully attached to the lower surface, but separated from the upper surface. The inverted base pressure is higher when activating only the upper AFC cylinder, so a separation bubble is formed on the upper surface, but the flow separates just downstream of the lower front edge. The inverted base pressure, $-Cpb$, is even higher when combining both upper and lower FC devices, so the flow on both upper and lower surfaces is attached (Fig. 15). The maximal value of $-Cpb$ is obtained when FC is not applied (Fig. 14c).

For $\theta = 75^\circ$, when the lower-front corner AFC device was activated, the inverse base pressure

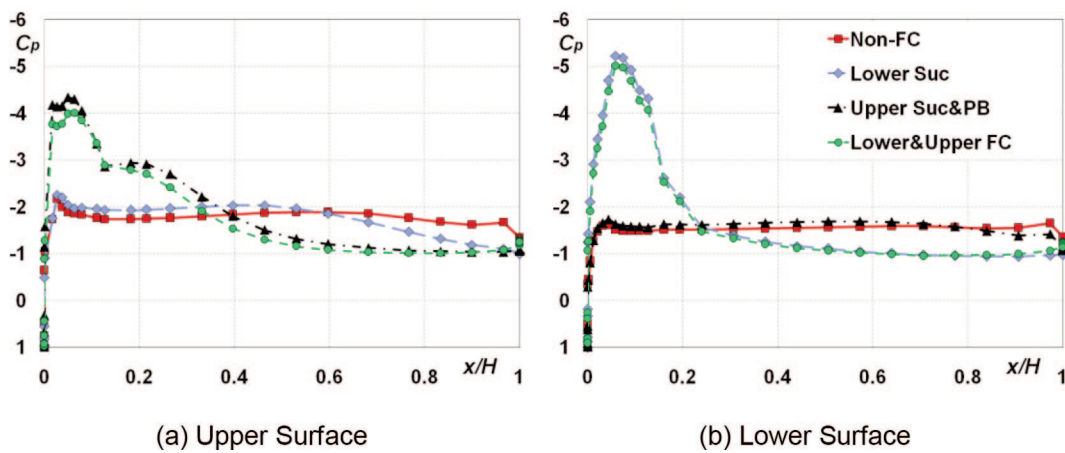


Figure 15. The pressure coefficient, C_p , vs. the normalized distance from the leading edge, x/H , for several FC configurations mentioned in the legend. a) The Upper surface of the model: $y/H > 0.5$. b) The lower surface of the model: $y/H < 0.5$. PBS location $\theta = 30^\circ$. $C_s = 0.0024$. $C_\mu = 0.014$. Two neighboring lower-front corner suction rows at $\gamma = 65^\circ$ & 73° are exposed to the flow. The valve is closed ($C_{sm} = 0$ or $C_\mu = 0$) when AFC is not applied. Reynolds number $Re = 0.2 \times 10^6$.

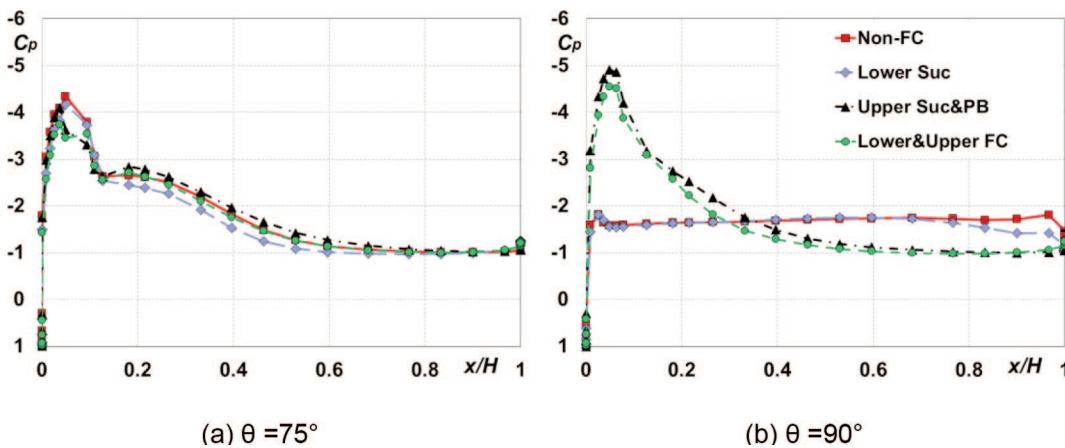


Figure 16. The pressure coefficient on the upper surface vs. normalized distance from the leading edge, x/H , for several FC configurations as indicated in the legend. a) $\theta = 75^\circ$. b) $\theta = 90^\circ$. Lower Fc device $C_s = 0.0024$. Upper AFC cylinder $C_\mu = 0.014$. Two neighboring lower-front-corner suction rows at $\gamma = 65^\circ$ & 73° are exposed to the flow. The valve is closed ($C_{sm} = 0$ or $C_\mu = 0$) when low surface FC is not activated. Reynolds number 0.2×10^6 .

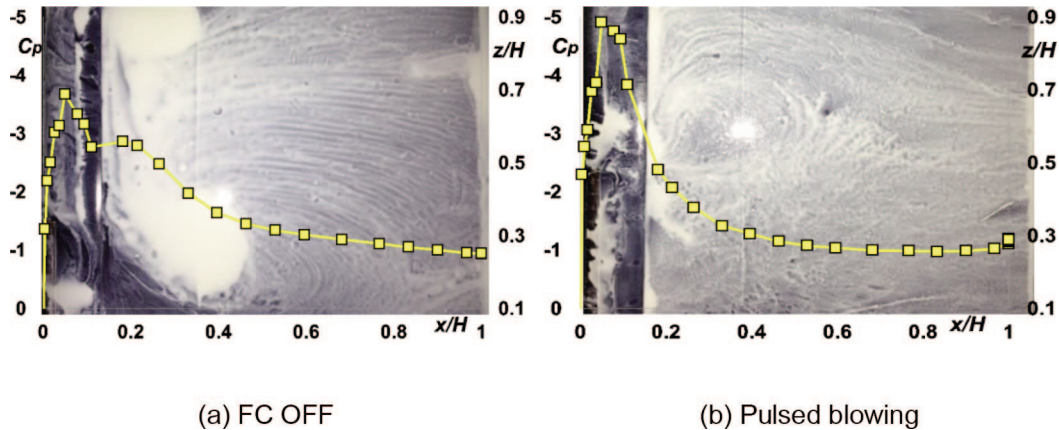


Figure 17. Pressure distributions (C_p vs. x/H) and corresponding oil flow visualization image of the upper surface. $Re = 0.4 \times 10^6$; Upper cylinder PBS location is $\theta = 15^\circ$; Lower FC pump openings are sealed ($C_{sm} = 0$), but its suction holes which are exposed to the flow are at $\gamma = 41^\circ$ & 32° . a) AFC is not applied. b) Pulsed blowing through the upper FC cylinder with nominal magnitude of $C_{\mu} = 0.014$ (upper cylinder suction holes are taped). Upper-front edge FC cylinder is shown between $x/H = 0$ and $x/H = 0.127$. The visualized range is about 40% of the wind tunnel model span (from the mid span to one of the wind tunnel vertical sidewalls). The secondary RHS axis refers to the normalized distance from the mid span of the model (span direction) of the flow visualization image (z/H).

increased (Fig. 14c). Observing Fig. 16a, the reason for this behavior could be explained as follows: Because of the strong passive effects of the upper cylinder FC exits for $\theta = 75^\circ$, the flow is accelerated, and a separation bubble is formed with or without front-upper AFC device activation. Therefore, when activating the suction on the lower-front edge surface, it acts to attach the flow (not shown). As a result, $-C_{pb}$ increases in the same manner described above. For $\theta = 90^\circ$, unlike the other PBS locations, it seems that when activating the upper-front AFC cylinder, a separation bubble is not formed, but the flow accelerates strongly. However, the inverse base pressure for this case is the same as for $\theta = 30^\circ$ where separation bubble was formed.

The findings of the current study were mainly obtained from the time-averaged pressure distributions around the model. According to the available information, some representative flow parameters were calculated including lift, drag, inverted base pressure, front side drag coefficient and the wake width. In order to obtain better understanding of the flow field, a flow visualization test was made, using a mixture of oil, kerosene and white pigment. The flow visualization images of the upper surface and corresponding pressure distributions are shown in Fig. 17.

Observing the flow visualization images, where FC is not applied (Fig. 17a), it can be noticed that a separation bubble was formed downstream of the front curved edge. Observing the corresponding pressure distribution it can be seen, in addition, that the pressure gradient corresponding to this region is indeed zero. This is an indication that the flow is separated, throughout this study. In addition, the bubble length of the oil flow image is in quite good agreement with the length of the zero pressure-gradient region in C_p . When pulsed blowing is applied on the upper surface, it acts to accelerate the flow in a stronger manner over the curved edge. Further downstream, the pressure recovers gradually. This is an indication that the flow is not necessarily separated. Observing the flow image for this case (Fig. 17b), it can be seen that indeed the separated area has vanished. However, as indicated earlier, the connection between the upper AFC cylinder to the model's surface is not perfectly smooth. Therefore, this area suffers from local short flow separation as can be seen from the surface flow image. The flow image shows also that the flow is characterized by three-dimensional structures, as typically found in similar massively separated flow conditions.

4. CONCLUSIONS

An AFC experiment applying active separation control devices to both front-rounded edges of a square prism was described. The effects of steady suction, oscillatory blowing and combining both techniques,

including the passive FC exits effects were studied. Both steady suction and pulsed blowing applied on the front round edge were found to be capable of reattaching separated flow around the curved regions and affect the flow parameters quite significantly. The suction and oscillatory blowing is achieved by a robust, no moving parts and easy to fabricate Suction and Oscillatory Blowing (SaOB) flow control actuator. The actuation on the front-edges acts for certain conditions, especially where the baseline flow is separated, to reduce the drag force by two mechanisms. The direct impact of the FC is to accelerate the flow, leading to a larger sub-pressure on the front side. Therefore, it is reasonable to assume that in practice, for a longer model (like heavy vehicle with a trailer), front AFC devices can be useful for drag reduction. In addition, AFC on the front side has the ability to delay separation or reattach separated flow and by that alter the flow over the horizontal surfaces downstream of the FC devices and in the near wake. This aspect needs to be further studied for a longer model. Additionally, further study should be performed to investigate the impact of the separation at the front-edges of the model and in the wake formation region downstream of it to identify physical mechanisms. The effect of AFC on square prism model with smaller radius at the front-edges and when the rear corners are rounded (with and without AFC) should be performed in conjunction with lower radius front corners.

ACKNOWLEDGMENTS

This project was partially supported by The Rinna Bolle Student Travel Fund of Tel Aviv University. Additionally, the authors would like to acknowledge support provided to this project by our International partners Mr. Linus Hjelm of Volvo Trucks and Mr. Oz Shamia of AFC Tech., Israel. The support of TAU Meadow Aerolab members: Vitali Palei, Victor Troshin, Tom Shtendel, Ori Friedland, Dima Sarkorov, Danny Dolgopyat, Artur Minasyan, Nir Morgolis and Nir Modanis is appreciated. Members of the Technical staff, lead by Mr. Shlomo Pasteur: Eli, Kronish, Avraham Blas, Shlomo Moshel, Shlomi Blaivis, Tomer Bachar and Mark Vassermann enabled this project. Partial financial support by the Meadow fund is appreciated.

REFERENCES

- [1] Hucho, W.-H., *Aerodynamics of road vehicles*, ed. W.-H. Hucho and S.R. Ahmed. 2002, London; Boston: Butterworths.
- [2] Choi, H., W.-P. Jeon and J. Kim, *Control of Flow Over a Bluff Body*. Annual Review of Fluid Mechanics, 2008. 40(1): p. 113–139.
- [3] Bellman, M., Naber, J. and Agarwal, R., *Numerical Drag Reduction Studies of Generic Truck Models Using Active Flow Control*. 39th AIAA Fluid Dynamics Conference 2009.
- [4] Arwatz, G., Fono, I. and Seifert, A., “Suction and Oscillatory Blowing Actuator Modeling and Validation”, *AIAA J.*, V. 40, N. 5, pp. 1007–1017, May 2008.
- [5] Shtendel, T. and Seifert, A., “Three-dimensional Aspects of bluff-body drag reduction by active flow control”, *Int. J. Heat and Flow*, Volume 45, February 2014, Pages 109–127. Prev. Shtendel, T. and Seifert, A., Drag Reduction of Bluff Body using Flow Control. 52nd ISR Aero Conf, Feb. 2012.
- [6] Wilson, J., Schatzmann, D., Arad, A., Seifert, A. and Shtendel, “Suction and Pulsed-Blowing Flow Control Applied to an Axisymmetric Body”, HYPERLINK "<http://arc.aiaa.org/loi/aiaaj>" *AIAA Journal*: 1-15, 10.2514/1.J052333, Posted online on 6 Aug 2013.
- [7] Schatzmann, D., J. Wilson, T. Shtendel, A. Seifert and E., Arad, “Flow Physics of Drag Reduction Mechanism Using Suction and Pulsed Blowing”, *AIAA J.* vol. 52, issue 11, pp. 2491-2505. Published Online Sept-2014. <http://arc.aiaa.org/doi/abs/10.2514/1.J052903> Prev. AIAA paper 1023-0488, 2013.
- [8] Lubinsky, G., *Flow Control Applied to the Front Edge of a Bluff Body*. 2013, M.Sc. Thesis, TAU: Tel-Aviv.
- [9] Lubinsky, G and Seifert, A. “Flow Control applied to the front rounded edge of a rectangular prism”, *Int. J of Flow Control*, May 2014. Previously presented at the 53rd Israel Annual Aerospace Conference, Feb. 2013.
- [10] Naim, A., Greenblatt, D., Seifert A. and Wygnanski, I., “Active Control of a Circular Cylinder Flow at Transitional Reynolds Numbers” (part of AIAA Paper 2002–3070), special Issue of Flow, Turbulence and Combustion on “Air-jet actuators and their use for flow control”, (2007), 78: 383–407.

